Published in final edited form as:

Clin Cancer Res. 2021 December 01; 27(23): 6467–6478. doi:10.1158/1078-0432.CCR-21-0544.

A Clinical PET Imaging Tracer ([^{18}F]DASA-23) to Monitor Pyruvate Kinase M2 Induced Glycolytic Reprogramming in Glioblastoma

Corinne Beinat[1,#], **Chirag B. Patel**[1,2,#], **Tom Haywood**[1], **Surya Murty**[1], **Lewis Naya**[2], **Jessa B. Castillo**[1], **Samantha T. Reyes**[1], **Megan Phillips**[2], **Pablo Buccino**[1], **Bin Shen**[1], **Jun Hyung Park**[1], **Mary Ellen Irene Koran**[3], **Israt S. Alam**[1], **Michelle L. James**[1,2], **Dawn Holley**[1], **Kim Halbert**[1], **Harsh Gandhi**[1], **Joy Q. He**[4], **Monica Granucci**[5], **Eli Johnson**[5], **Daniel Dan Liu**[4], **Nobuko Uchida**[4], **Rahul Sinha**[4], **Pauline Chu**[6], **Donald E. Born**[7], **Geoffrey I. Warnock**[8], **Irving Weissman**[4], **Melanie Hayden-Gephart**[5], **Mehdi Khalighi**[1], **Tarik F. Massoud**[1,9], **Andrei Iagaru**[3], **Guido Davidzon**[3], **Reena Thomas**[2], **Seema Nagpal**[2], **Lawrence D. Recht**[2], **Sanjiv Sam Gambhir**[1,10]

[1]Department of Radiology, Molecular Imaging Program at Stanford, Stanford University School of Medicine, Stanford, CA 94305, USA.

[2]Department of Neurology and Neurological Sciences, Stanford University School of Medicine, Stanford, CA 94305, USA.

[3]Division of Nuclear Medicine and Molecular Imaging, Department of Radiology, Stanford University, Stanford, CA 94305, USA.

[4]Stanford Institute for Stem Cell Biology and Regenerative Medicine, Department of Pathology, Stanford University School of Medicine, Stanford, CA, 94305, USA

[5]Department of Neurosurgery, Stanford University School of Medicine, Stanford, CA, 94305, USA

[6]Stanford Human Research Histology Core, Stanford University School of Medicine, Stanford, CA, 94305, USA

[7]Department of Pathology, Neuropathology, Stanford University School of Medicine, Stanford, CA, 94305, USA

[8]PMOD Technologies Ltd, Zurich, Switzerland

[9]Division of Neuroimaging and Neurointervention, Department of Radiology, Stanford University School of Medicine, Stanford, CA, 94305, USA

[10]Departments of Bioengineering and Materials Science & Engineering, Stanford University, Stanford, CA 94305, USA.

Abstract

Correspondence to: Corinne Beinat, 318 Campus Drive, Stanford CA 94305, +1 650-725-3113, cbeinat@stanford.edu, Lawrence Recht, 875 Blake Wilbur, Stanford CA 94305, +1 650-725-8630, lrecht@stanford.edu.
[#]Authorship note: CB and CBP contributed equally to this work

Conflict of interest: the authors declare no conflict of interest

Purpose: Pyruvate kinase M2 (PKM2) catalyzes the final step in glycolysis, a key process of cancer metabolism. PKM2 is preferentially expressed by glioblastoma (GBM) cells with minimal expression in healthy brain. We describe the development, validation, and translation of a novel positron emission tomography (PET) tracer to study PKM2 in GBM. We evaluated 1-((2-fluoro-6-[^{18}F]fluorophenyl)sulfonyl)-4-((4-methoxyphenyl)sulfonyl)piperazine ([^{18}F]DASA-23) in cell culture, mouse models of GBM, healthy human volunteers, and GBM patients.

Experimental Design: [^{18}F]DASA-23 was synthesized with a molar activity of 100.47 ± 29.58 GBq/μmol and radiochemical purity >95%. We performed initial testing of [^{18}F]DASA-23 in GBM cell culture and human GBM xenografts implanted orthotopically into mice. Next we produced [^{18}F]DASA-23 under FDA oversight, and evaluated it in healthy volunteers, and a pilot cohort of glioma patients.

Results: In mouse imaging studies, [^{18}F]DASA-23 clearly delineated the U87 GBM from surrounding healthy brain tissue and had a tumor-to-brain ratio (TBR) of 3.6 ± 0.5. In human volunteers, [^{18}F]DASA-23 crossed the intact blood-brain barrier and was rapidly cleared. In GBM patients, [^{18}F]DASA-23 successfully outlined tumors visible on contrast-enhanced magnetic resonance imaging (MRI). The uptake of [^{18}F]DASA-23 was markedly elevated in GBMs compared to normal brain, and it identified a metabolic non-responder within 1-week of treatment initiation.

Conclusion: We developed and translated [^{18}F]DASA-23 as a new tracer that demonstrated the visualization of aberrantly expressed PKM2 for the first time in human subjects. These results warrant further clinical evaluation of [^{18}F]DASA-23 to assess its utility for imaging therapy-induced normalization of aberrant cancer metabolism.

Keywords

pyruvate kinase M2; glioblastoma; glycolysis; [^{18}F]DASA-23

Introduction

Enhanced glucose uptake is a hallmark of multiple cancers and has been developed as a clinical diagnostic tool through positron emission tomography (PET) imaging of the radiolabeled glucose analog, 2-[^{18}F]fluoro-2-deoxy-D-glucose ([^{18}F]FDG) (1, 2). [^{18}F]FDG is an indispensable tool in oncology for the staging and restaging of cancer, detection of recurrence, monitoring of treatment response, and facilitating timely modifications of therapeutic strategies (3, 4). Unfortunately, high background signal from glucose metabolism within the healthy brain limits the diagnostic utility of [^{18}F]FDG in brain cancers (5-7). Radiolabeled amino acids represent another class of PET tracers used in the evaluation of brain cancers. They have shown improved utility for imaging brain tumors due to the increased uptake in tumor tissue, low uptake in healthy brain tissue, and include [^{11}C]-methionine, L-3,4-dihydroxy-6-[^{18}F]-fluorophenyl-alanine ([^{18}F]FDOPA), and [^{18}F]-fluoroethyltyrosine ([^{18}F]-FET) (8-12). Their uptake is predominantly mediated by the L-type amino acid transporter (LAT) and generally reflects nutrient uptake to support increased biomass and proliferative energy demands (6, 13). Indeed, these agents provide important

diagnostic information regarding delineation of tumor extent, diagnosis of treatment-related changes, and assessment of treatment response. But, given the key role of glycolysis in cancer cell metabolism and response to therapy (14), brain cancers would benefit from non-invasive imaging of glycolysis.

Pyruvate kinase (PK) catalyzes the conversion of phosphoenolpyruvate to pyruvate, simultaneously producing adenosine triphosphate (ATP) (Fig. 1A) (15). The expression of the pyruvate kinase M2 (PKM2) isoform is reported to contribute to the distinctive glycolysis in cancers, and replacement of PKM2 with its splice variant, PKM1, results in insufficient biosynthesis, thus inhibiting cancer growth (16). PKM1 is present in differentiated tissues including the brain, while PKM2 is found in most proliferating cells, including the majority of cancer cell lines and malignancies studied to date. PKM1 has high constitutive enzymatic activity, whereas PKM2 is allosterically regulated through the stabilization of a highly active tetramer relative to the inactive dimeric PKM2 (17, 18). The reduced activity of dimeric PKM2 results in a diminished production of pyruvate, enabling accumulation of upstream glycolytic intermediates and a metabolic shift towards an anabolic state (18). The dynamic equilibrium between the dimeric and tetrameric states of PKM2 enables proliferating cancer cells to regulate their needs for anabolic and catabolic metabolism and, to favor high levels of dimeric PKM2 (19). The Warburg effect is therefore partly mediated by PKM2 expression, with high expression of dimeric PKM2 in cancer cells contributing to anabolic glucose metabolism, promoting macromolecular biosynthesis, and benefiting cancer cell proliferation and growth (20). To date, there have been no reports of radiopharmaceuticals that can provide a non-invasive measure of PKM2 status in human subjects.

Glioblastoma (GBM) is the most common and lethal primary central nervous system cancer in adults (21). It is a WHO grade IV glioma representing approximately 15% of all primary intracranial malignancies (21). Despite aggressive surgical resection, radiotherapy and chemotherapy, prognosis remains dismal with overall survival of newly diagnosed GBMs being only ~5% at 5 years after diagnosis (21). PKM2 expression in gliomas is well established; grade I-III gliomas exhibit modestly increased levels of PKM2 protein expression relative to normal brain tissue. GBM displays a further 4- to 5-fold increase in PKM2 protein expression (22). Given the absence of PKM2 in healthy brain and its role in glucose metabolism, PKM2 represents an attractive imaging target for investigating patients with GBM and other brain malignancies. Our group has previously reported the development of 1-((2,6-difluorophenyl)sulfonyl)-4-((4-(methoxy-[^{11}C])phenyl)sulfonyl)piperazine ([^{11}C]DASA-23) as a novel radiotracer that provided a direct measure of PKM2 in pre-clinical models of GBM (23). These studies demonstrated the *in vitro* and *in vivo* specificity of [^{11}C]DASA-23 for the detection of PKM2 (23). Owing to the favorable properties of fluorine-18 for clinical translation, we subsequently reported the radiosynthesis of 1-((2-fluoro-6-[^{18}F]fluorophenyl)sulfonyl)-4-((4-methoxyphenyl)sulfonyl)piperazine ([^{18}F]DASA-23), an isotopologue PKM2-specific radiotracer (Fig. 1A) (24-26). In this study, we report the pre-clinical development and initial clinical evaluation of [^{18}F]DASA-23 to image PKM2 status in patients with GBM.

Materials and Methods

Cell lines

We purchased LN18, U87, and U87 IDH1R132H cells from ATCC (Manassas, VA) and maintained them in culture according to the manufacturer's protocol. We generated U87-GFP/luc by transduction with a lentiviral vector that expressed a fusion protein of green fluorescent protein (GFP) and firefly luciferase (luc) followed by puromycin selection (125 ng/mL). We received GBM206 cells as a gift from Professor Jann Sarkaria (Mayo Clinic). Mycoplasma testing was performed on a monthly basis. Cells were kept within 15 passages of the original frozen vial and authenticated using short tandem repeat profiling.

After obtaining informed consent under Stanford IRB protocol 12625, we acquired patient tissue used to generate the human glioblastoma cell line TP459 through Stanford IRB protocol 34363. We obtained a single cell suspension of TP459 cells by mechanical dissociation using a scalpel, followed by enzymatic dissociation using DNAse I (250 U/mL, DPRFS Worthington, NJ) and Liberase TM (LIBTM-RO, Sigma Aldrich, St. Louis, MO) on a shaker at 37 °C. Following enzymatic digestion, a Percoll gradient was used to separate myelin. We depleted red blood cells using a density gradient (Histopaque 1119, Sigma Aldrich). The remaining cell suspension was then harvested, washed, and stained with anti-human CD45 antibody conjugated to phycoerythrin using a 1:20 ratio (5 μL in 100 μL staining solution) (Clone HI30, BD Biosciences, San Jose, CA) followed by anti-PE microbeads using a 1:5 ratio (20 μL in 100 μL staining solution) (130-048-801, Miltenyi, Sunnyvale, CA). We collected CD45- cells *via* magnetic separation and transferred to tissue culture flasks for *in vitro* culture at 37 °C and 5% CO_2. We maintained TP459 cells in culture as a neurosphere suspension in serum free medium.

Radiosynthesis of [^{18}F]DASA-23

We completed the radiosynthesis of [^{18}F]DASA-23 per previously reported methods (24).The radiochemical yield was 1.68 ± 0.92 %, non-decay corrected at end of synthesis and the molar activity was 100.47 ± 29.58 GBq/μmol (n=15).

Cell uptake studies

We plated all cells (2×10^5 per well) in 12-well plates the day before uptake studies. Cell uptake studies using U87, U87 IDH1R132H, LN18, GBM206, and TP459 cell lines were performed per previously reported methods (25, 26). TP459 neurospheres were processed into single cell suspensions prior to plating following treatment with Accustase (A1110501, Thermo Fisher Scientific Inc., Waltham, MA).

Intracranial tumor model

We obtained approval for all experimental procedures involving animals from the Stanford University Institutional Animal Care and Use Committee under protocol 12040. Orthotopic brain tumor models were completed according to previously described methods (23). We implanted 4×10^5 U87 cells in the right hemisphere, 0.5 mm anterior and 2 mm lateral to the skull lambda, in the brains of 6- to 8-week-old nude mice held in place with a stereotaxic frame. Cells were suspended in 3 μL of Hank's balanced salt solution (HBSS)

and were injected at a depth of 3 mm over 5 min using a Hamilton syringe, which was subsequently held in place for a further 2 min. We subsequently imaged tumor-bearing mice approximately 21 days after intracranial injection.

Animal imaging studies

We completed magnetic resonance imaging (MRI) studies at the Stanford Small Animal Imaging facility using a Discovery MR901 General Electric 7T horizontal bore scanner (GE Healthcare, Chicago, IL) according to previously described methods (23). We completed small animal PET imaging scans on a docked Siemens Inveon PET/CT scanner (matrix size 128 × 128 × 159; CT attenuation corrected; non-scatter corrected) after a bolus of intravenous injection of 8 ± 0.9 MBq [^{18}F]DASA-23 in approximately 150 μL. We acquired dynamic scans in listmode format over 30-60 min. The acquired data were then arranged into 0.5 mm sonogram bins and 15-19 frames for image reconstruction (4 × 15 s; 4 × 60 s, and 11 × 300 s). The densities were averaged for all regions of interest at each time point to compute a time-activity curve. We normalized tumor and tissue time-activity curves to the injected amount of radioactivity and expressed values as %ID/g, assuming 1 g/mL. The normalized uptake of radiotracer at 30 min within the healthy contralateral region of the brain was used for comparison. We completed PET/MR registration in Inveon Research Workplace (IRW) (Siemens, Munich, Germany) software and used the CT image for alignment of the skull. The CT intensity was then lowered to allow visualization of fused PET/MR images. We used IRW for visualization of radiotracer uptake within the tumor, to define the volumes of interest and to create the images. Tumor [^{18}F]DASA-23 uptake was quantified using threshold-based 3D volume of interest (VOI) in IRW. VOIs were defined on summed images for 10-30 min post-injection and transferred to the dynamic images to determine time-activity curves.

Autoradiography

We completed autoradiography per previously described methods (27). For blocking studies, we administered [^{18}F]DASA-23 1 h after intraperitoneal injection of TEPP-46 (50 mg/kg in 40% w/v (2-hydroxypropyl)-b-cyclodextrin in PBS; Cayman Chemical, Ann Arbor, MI). Thirty min after injection of radioactivity, we transcardially perfused mice with saline (15 mL) and the brain embedded in optimal cutting temperature (OCT) and processed for autoradiography according to published methods (27).

Immunofluorescence

We stained whole tissue sections with hematoxylin and eosin (H&E) and anti-PKM2 immunofluorescence according to published methods (26).

Mouse brain processing and evaluation of PKM2 levels

We orthotopically implanted nude mice (n=4) with U87-GFP/luc glioma cells as previously described (23). After 21 days of tumor implantation, the brain was rapidly removed and placed into ~5 mL ice cold HBSS containing HEPES (12.5 mL 1M HEPES per 487.5 mL HBSS). We homogenized the brains and passed the homogenate through a 40 μm cell strainer. The sample was centrifuged at 300*g* for 5 min at 4 °C to remove excess

buffer, then re-suspended in a standard isotonic percoll solution, and centrifuged at 800*g* for 20 min at 4 °C to remove myelin. We then re-suspended cells in 2% bovine serum albumin (BSA) in PBS and stained with antibodies for flow cytometry analysis. Cell surface marker antibodies were added at a concentration of 0.2 μg per 1×10^6 cells in 100 μL volume. Antibodies included anti-CD45 (30F11, Biolegend, San Diego, CA), and anti-CD11b (M1/70, Biolegend) and anti-PKM2 (D78A4, Cell Signaling Technologies). We washed all samples and then analyzed them using a FACSAria II (BD Bioscience, San Jose, CA). We analyzed the data using FlowJo. We first gated cells using forward scatter and side scatter. We then gated immune cells on CD11b and CD45, while tumor cells were gated based on GFP signal.

Determination of IC_{50} values

We purchased TMZ from SellekChem (Houston, TX) and determined the IC_{50} value in TP549 cells according to reported methods (25).

Study Subjects

Healthy Volunteers (Stanford PET/MRI Metabolic Service Center)—This clinical trial (NCT03539731) was approved by the local Institutional Review Board (IRB-44597) and the local Cancer Center's scientific review committee (BRN0038), and is compliant with federal, state, and local regulation on medical research, and with the 1964 Helsinki declaration and its later amendments or comparable ethical standards. We obtained written informed consent from all individual participants. Inclusion criteria included age ≥ 18 years, adequate organ function as assessed by blood analysis up to 14 days prior to the [^{18}F]DASA-23 PET/MRI scan and defined by absolute neutrophil count (ANC) ≥ 1.5×10^9/L without myeloid growth factor support; hemoglobin (Hgb) ≥ 9 g/dL; platelet count ≥ 100 × 109/L; bilirubin ≤ 1.5 × upper limit of normal (ULN) except for documented history of Gilbert's disease; alanine aminotransferase (ALT) and aspartate aminotransferase (AST) each ≤ 2.5 × ULN; alkaline phosphatase (AP) ≤ 3 × ULN; and in women of childbearing potential, a negative serum pregnancy test. Exclusion criteria included pregnant and nursing participants, implanted devices contraindicated for MRI, pre-specified co-morbid diseases, incurrent illness, prior or current malignancy, known kidney disease, and history of allergic reactions to skin adhesives (e.g. tapes) used in medical care. We requested no specific patient preparation (i.e., fasting) prior to the [^{18}F]DASA-23 PET/MRI scan. We monitored vital signs, including heart rate, pulse oximetry, and body temperature, pre- and post-administration of [^{18}F]DASA-23. To evaluate toxicity of the injected dose of [^{18}F]DASA-23, we obtained blood specimens (complete blood count with differential and complete metabolic panel) from each participant and analyzed before and within 7 days post injection of [^{18}F]DASA-23. Adverse events were recorded on the day of imaging as well as during follow-up up to 7 days.

Brain Tumor Patients (Stanford PET/MRI Metabolic Service Center)—Inclusion criteria included age ≥ 18 years, adequate organ function as assessed by blood analysis within 14 days prior to the [^{18}F]DASA-23 PET/MRI scan, a negative pregnancy test in women of childbearing potential, and any of the following: (a) radiographical or pathological evidence of newly-diagnosed intracranial tumor that was status-pre surgical

resection; (b) radiographical or pathological evidence of progressive/recurrent intracranial tumor; (c) question of pseudoprogression versus true progression on the most recent standard-of-care brain MRI; or (d) evidence on the most recent standard-of-care brain MRI scan of intracranial metastasis/metastases in a patient with known extracranial primary cancer. Exclusion criteria included pregnant and nursing participants, implanted devices contraindicated for MRI, pre-specified co-morbid diseases, incurrent illness, known kidney disease, history of allergic reactions to skin adhesives, and other chemotherapy (besides what was being used to treat the intracranial tumor).

Clinical PET Imaging and Reconstruction—Whole body tracer distribution was assessed in a cohort of healthy volunteers (Group I, NCT03539731) using serial PET/MRI scans on a time-of-flight simultaneous PET/MRI scanner (SIGNA PET/MRI; GE Healthcare, Waukesha, WI, USA) as previously described (28). Brain tumor patients (Groups II and III, NCT03539731) and an additional cohort of healthy volunteers (Group IV, NCT03539731) underwent 60-min brain acquisitions, a dynamic emission acquisition sequence in 3-dimensional mode over 60 min was started immediately prior to intravenous administration of [^{18}F]DASA-23. Participants received 294 ± 12 MBq of [^{18}F]DASA-23. We reconstructed the PET data using a fully 3-dimensional iterative ordered subsets expectation maximization algorithm (28 subsets, 2 iterations) and corrected for attenuation, scatter, dead time, and decay. We applied MR-based ZTE attenuation correction and reconstructed the image into the following frames: 8 × 15 s; 16 × 30 s, 20 × 60 s, 10 × 200 s and 2 × 300 s. We completed a standardized brain tumor MRI protocol (29). Per standard of care, 330 MBq of [^{18}F]FDG was administered to patient IC-1. Approximately 45 min after intravenous administration of [^{18}F]FDG, a plain CT was obtained from the vertex to the skull base in 3D model for use in attenuation correction and anatomic localization of radiotracer activity. Emission scans were completed over the same anatomical regions. [^{18}F]FDG PET images were retrospectively accessed, reconstructed, and reviewed in the axial, coronal and sagittal planes under IRB protocol 42357.

Image Analysis Healthy Volunteers—The whole-body dosimetry of [^{18}F]DASA-23 was assessed as described previously (28). The brain distribution and kinetics of [^{18}F]DASA-23 were assessed using a brain region atlas approach implemented in the PMOD PNEURO tool. The anatomical MRI was segmented and matched to a template before transferring the atlas regions to the PET data. Regional time-activity curves were extracted and adjusted for injected dose and body weight by calculating SUV.

Image Analysis Brain Tumor Patients—Tumor [^{18}F]DASA-23 uptake was quantified using threshold-based 3D VOIs in the PMOD PFUS tool. VOIs were defined on summed images for 30-60 min post-injection and transferred to the dynamic image series to extract time-activity curves. Tumor VOIs were defined using a 70% peak-voxel activity isocontour. The normal white-matter reference brain region for tumor-to-brain calculation was the contralateral centrum semiovale. The SUV in gray matter was measured using manually drawn VOIs along the cortical band of the contralateral frontal and parietal cortices. Ratios of tumor uptake were defined as tumor-to-brain ratio (TBR), tumor-to-brain maximum ratio (TBRmax) and tumor-to-gray matter ratio. SUV histograms for the tumors in IC-1 to IC-4

were calculated by extracting the voxel values for voxels within the 70% peak voxel activity isocontour VOI using the Pixeldump functionality in PMOD.

Tissue homogenization and western blot analysis—We obtained informed consent under IRB protocol 12625, and then obtained patient tissue used to evaluate PKM2 expression by western blot through Stanford IRB protocol 34363. We homogenized tissues on ice in RIPA buffer (89900, Thermo Fisher Scientific Inc.) containing 1X Halt protease inhibitors (78429, Thermo Fisher Scientific Inc.). We prepared the U87 cell lysate by lysing U87 cells in RIPA buffer containing protease inhibitors for 10 min on ice. We determined the protein concentration of these samples using the BCA assay and evaluated the cellular lysates for PKM2 protein expression using a standard western blotting protocol (25).

Immunohistochemistry—Under IRB protocol 42357, we obtained formalin-fixed paraffin-embedded brain tumor tissue. The specimens were reviewed with a neuropathologist to identify regions of neoplasm and these regions were sectioned at 5 μm. Adjacent sections were stained with standard H&E and, following antigen retrieval at pH 6.0, by immunohistochemistry for PKM2 (1:600, D78A4 XP® Rabbit mAb [Cell Signaling Technologies catalog #4053]) . We scanned the slides on a digital pathology slide scanner (Aperio, Leica Biosystems) and images were viewed using Aperio ImageScope version 12.4.0.5043 (Leica Biosystems).

Statistics—Data analysis and visualization was performed using Prism 7.0 (Graphpad Software). All data are presented as the average value ± the standard deviation of at least three independent measurements. Statistical analysis for cell and animal studies were performed by Student's t-test and one way ANOVA using Prism as indicated in the figure legends. Multiple comparisons were assessed using the Tukey's multiple comparisons test. Significance was assigned for p values of <0.05.

Results

Pre-clinical validation of [^{18}F]DASA-23

We radiolabeled DASA-23 with fluorine-18 in the native position of fluorine on the DASA-23 molecule; as reported previously (Supplemental Fig. 1) (24), and obtained [^{18}F]DASA-23 with a radiochemical yield of 1.68 ± 0.92%, molar activity of 100.47 ± 29.58 GBq/μmol and chemical and radiochemical purity >95% (n=15). We performed initial cellular uptake studies in human GBM cell lines possessing diverse molecular characteristics, namely isocitrate dehydrogenase 1 (IDH1) mutation and methylguanine-DNA methyltransferase (MGMT) promoter methylation status. Rapid and extensive cellular uptake was observed in all GBM lines evaluated after addition of [^{18}F]DASA-23. At 30 min after addition of radioactivity, the highest uptake values were evident in U87 (IDH1 wildtype, and MGMT promoter methylated) and LN-18 (IDH1 wildtype, and MGMT promoter unmethylated) cells, reaching 25.3 ± 7.2% and 23.9 ± 1.4% uptake/mg protein, respectively (Fig. 1B). This was followed by U87 IDH1 R132H (MGMT promoter methylated) and patient-derived GBM206 (IDH1 wildtype, and MGMT promoter methylated) cells that reached [^{18}F]DASA-23 uptake values of 15.9 ± 3.6% uptake/mg

protein and 15.5 ± 3.0% uptake/mg protein, respectively. [^{18}F]DASA-23 uptake continued to increase over the 60-min incubation period in all cell lines evaluated. Removal of exogenous radioactivity resulted in the efflux of cell-associated activity, with ~42% retention of the initial intracellular radioactivity remaining 30 min after removal of exogenous [^{18}F]DASA-23 for all cell lines (Fig. 1B).

In view of the favorable cancer cell uptake of [^{18}F]DASA-23, we assessed the potential use of this tracer for *in vivo* imaging of PKM2 status. We first assessed the brain penetrance and biodistribution of [^{18}F]DASA-23 using small animal PET/CT imaging of healthy nude mice. Dynamic imaging following intravenous administration of ~8 MBq [^{18}F]DASA-23 revealed it passively crossed the intact blood-brain barrier (BBB), with peak uptake levels of 8.6 ± 0.6 %ID/g (n=4) occurring at ~1 min after tracer administration (Fig 1D). Subsequently, [^{18}F]DASA-23 radioactivity within the healthy brain rapidly cleared over the 60-min acquisition period, with low levels remaining at 30 min and 60 min after tracer administration (0.8 ± 0.1 %ID/g and 0.7 ± 0.1 %ID/g, respectively) (Fig. 1D). The clearance of [^{18}F]DASA-23 was predominantly found to be through renal and hepatobiliary pathways (Fig. 1E).

Owing to the low levels of tracer accumulation within healthy brain, we were motivated to explore the ability of [^{18}F]DASA-23 to measure PKM2 status in mice orthotopically implanted with human U87 GBMs genetically modified to express green fluorescent protein and firefly luciferase (U87-GFP/luc). We used T2-weighted magnetic resonance imaging (MRI) to confirm the presence of the intracranial tumor in each mouse (Fig. 2A). Small animal PET imaging following intravenous administration of [^{18}F]DASA-23 (~8 MBq) allowed clear visualization of aberrantly expressed PKM2 within the brain tumors (Fig. 2A). The kinetics of [^{18}F]DASA-23 within the U87-GFP/luc tumors consisted of rapid tracer delivery followed by slow washout (Fig. 2B). At 30 min post radiotracer administration, the levels of radioactivity within the U87-GFP/luc GBMs were 1.9 ± 0.4 %ID/g, which were significantly higher than those of the contralateral normal brain (0.6 ± 0.1 %ID/g, $p<0.0001$, n=8, Fig. 2C), establishing a tumor-to-brain ratio (TBR) of 3.6 ± 0.5. We compared the ability of [^{18}F]DASA-23 to delineate orthotopic U87-GFP/luc GBMs compared to an established amino acid PET agent, 3,4-dihydroxy-6-[^{18}F]-fluoro-l-phenylalanine ([^{18}F]FDOPA) currently explored in the clinical management of GBM patients (30). Similar to [^{18}F]DASA-23, [^{18}F]FDOPA delineated the orthotopically implanted U87-GFP/luc GBMs (Supplemental Fig. 2) with a TBR of 2.5 ± 0.3 (n=4) at 30 min after tracer administration.

After [^{18}F]DASA-23 PET imaging we excised brains of tumor-bearing mice for analysis using *ex vivo* autoradiography and histopathology. Similar to the PET images, *ex vivo* autoradiography revealed the radioactive signal within the U87-GFP/luc GBMs to be clearly defined from the surrounding brain tissues (Fig. 2D). Hematoxylin and eosin (H&E) staining of adjacent sections demonstrated the presence of highly cellular tumor tissue with good localization to [^{18}F]DASA-23 autoradiography (Fig. 2E). Immunofluorescence staining of PKM2 within adjacent tumor sections revealed excellent correlation with the GFP-positive U87 cells and cytosolic PKM2 expression (Supplemental Fig. 3A-B). PET imaging and autoradiography completed under blocking conditions with structurally distinct

PKM2 activator TEPP-46 (50 mg/kg) attenuated the [^{18}F]DASA-23 signal within the U87 GBMs at 30 mins post injection, highlighting the *in vivo* specificity of [^{18}F]DASA-23 for PKM2 (Supplemental Fig. 3C-E). We additionally processed the brains of U87-GFP/luc tumor-bearing mice (n=4) for analysis of PKM2 levels in multiple cell populations within the tumor microenvironment using flow cytometry. This revealed PKM2 expression was almost exclusively found in U87 GFP-positive cancer cells with minimal PKM2 found in infiltrating myeloid, microglial, or lymphoid cell populations (Fig. 2F). Collectively, these data highlight the potential for clinical translation of [^{18}F]DASA-23 to evaluate PKM2 status in patients harboring GBMs.

[^{18}F]DASA-23 in healthy human volunteers

We intravenously administered [^{18}F]DASA-23 to four healthy male and two healthy female adult volunteers to study radiation dosimetry and brain kinetics using simultaneous PET/MRI (Supplementary Table 1). We noted no adverse events at the time of imaging or after 7 days; the effective dose of [^{18}F]DASA-23 was 23.5 ± 5.8 μSv/MBq (28). The pharmacokinetics and biodistribution of [^{18}F]DASA-23 in a healthy volunteer (at 0.5, 1, 2 and 3 h after administration) are shown in Fig. 3A. The dose-limiting organ was determined to be the gallbladder, which received an absorbed dose of 0.61 ± 0.52 mSv/MBq (28). We evaluated brain uptake patterns of [^{18}F]DASA-23 over the course of a 60 min brain acquisition beginning with intravenous administration of [^{18}F]DASA-23 (Fig. 3B). The tracer exhibited high initial localization (peak SUV ~ 5) to most brain structures, including cerebral cortex (Fig. 3C) and the posterior fossa (Fig. 3D), followed by rapid washout over the 60 min acquisition period. This was in contrast to white matter, which was characterized by lower delivery of the tracer (peak SUV ~ 2) and slower washout (Fig. 3E).

Evaluation of [^{18}F]DASA-23 PET/MRI in glioma patients

We intravenously administered ~300 MBq [^{18}F]DASA-23 to two female and two male patients diagnosed with malignant gliomas, and completed a 60-min dynamic brain acquisition using simultaneous PET/MRI (Supplemental Tables 2-6). There were no adverse clinical reactions to [^{18}F]DASA-23 injections. Representative decay-corrected time-activity curves for the tumor, centrum semiovale (white matter), and the contralateral frontal, and parietal cortices (gray matter [GM]) were averaged for patients undergoing [^{18}F]DASA-23 PET imaging (Supplemental Fig. 4). We used this information to select the timeframe for obtaining a suitable ratio of tumor uptake relative to normal brain tissue. The optimal timeframe was determined to be 30-60 min after radiotracer administration, with the criterion that any tracer accumulation above background was considered abnormal. We used white matter at the level of the contralateral centrum semiovale as the reference region for tumor-to-brain ratio (TBR) calculations. The corresponding SUV, SUV max, TBR, TBR max, and tumor-to-gray matter (T/GM and T/GM max) values are summarized in Table 1.

The first patient (intracranial patient one, IC-1) was diagnosed with recurrent GBM, having IDH wild-type and methylated MGMT promoter status. Contrast enhanced MRI revealed a large enhancing tumor within the left frontal lobe (Fig. 4A). Dosages of 337 MBq [^{18}F]FDG and 300 MBq [^{18}F]DASA-23 were administered to the patient on separate days. [^{18}F]FDG PET/CT revealed subtle although asymmetric [^{18}F]FDG uptake corresponding to the region

of MRI enhancement (Fig. 4B and Table 1). [^{18}F]DASA-23 clearly delineated this lesion within the left frontal lobe with a TBR max of 2.6 (Fig. 4C and Table 1). The patient then began treatment with bevacizumab (7.5 mg/kg) and temozolomide (TMZ) chemotherapy (150 mg/m^2), and we then obtained a second [^{18}F]DASA-23 PET/MRI 6 days later to detect early metabolic treatment response (Fig. 4D-E). We compared that result with the outcome noted at 3 months (Fig. 4F). In the post-therapy [^{18}F]DASA-23 PET, we observed an increased TBR max of 2.9 (Fig. 4D and G, Table 1). We observed a discordance between [^{18}F]DASA-23 PET and MRI, the latter of which demonstrated a reduction in contrast-enhancing tumor volume after administration of bevacizumab and TMZ. We also noted that the highest levels of [^{18}F]DASA-23 tracer uptake in both pre- and post-therapy scans were observed in the posterior medial aspect of the left frontal mass, which did not exhibit substantial contrast enhancement on both the pre- and post-therapy MRI scans (Supplemental Fig. 5). A standard of care MRI three months after [^{18}F]DASA-23 PET revealed progressive disease within the areas of [^{18}F]DASA-23 uptake at the medial and lateral posterior portions of the GBM (Fig. 4F), and the patient subsequently underwent tumor re-resection. H&E staining and immunohistochemistry (IHC) of the resected tissue confirmed the expression of PKM2 in the cancer cells shown in the adjacent tissue sections, Figs. 4H-I. Low levels of PKM1 were detected within the cancer cells (Supplemental Fig. 5). Western blot analysis additionally confirmed the presence of PKM2 within the resected tissue compared to a non-matched normal brain sample and U87 cell lysate (Supplemental Fig. 6). We developed a primary patient-derived cell line (TP459) from IC-1's tumor tissue, maintained it in culture as neurospheres, and subsequently confirmed the cellular uptake of [^{18}F]DASA-23 in the *ex vivo* cultured cells (Fig. 4J). We also subjected TP459 cells to the IC_{50} dosage of TMZ for 72 h (Supplemental Fig. 7A), and then assessed uptake of [^{18}F]DASA-23 (Fig. 4J). There was a non-significant difference between [^{18}F]DASA-23 uptake in untreated TP459 cells and TMZ-treated TP459 cells (29.5 ± 2.3 %uptake/mg protein vs. 26.1 ± 1.9 %uptake/mg protein, p=0.12) from this patient who was treated with TMZ and did not respond. We confirmed *via* western blot that there was a non-significant different in PKM2 protein expression between untreated and TMZ-treated TP459 cells (Supplemental Fig. 7B-C).

Intracranial patient 2 (IC-2) was diagnosed with GBM, having IDH1 wild-type and unmethylated MGMT promoter status. Contrast enhanced MRI revealed a heterogeneous, enhancing GBM centered in the left body of the *corpus callosum*, with involvement of the left frontal lobe, corona radiata, and with contralateral extension shown in the coronal image in Fig. 5A. This patient was receiving bevacizumab therapy at the time of [^{18}F]DASA-23 PET/MRI, an infusion of 7.5 mg/kg was completed 14 days prior to the [^{18}F]DASA-23 PET/MRI. [^{18}F]DASA-23 targeted and outlined this tumor (Fig. 5B), with homogeneous uptake of the tracer observed within the lesion compared to the heterogeneous MRI contrast enhancement (Fig. 5C). [^{18}F]DASA-23 PET revealed high levels of tracer avidity and metabolic activity within this tumor, with TBR max of 2.8 (Table 1 and Supplemental Figure 8). H&E staining and IHC analysis of the biopsied tissue confirmed that the GBM cells expressed PKM2 (Fig. 5D-G). Low levels of PKM1 were found within the lesion (Supplemental Fig. 8).

We also administered [^{18}F]DASA-23 to one patient diagnosed with WHO Grade IV diffuse midline glioma, H3 K27M-mutant (IC-3). At the time of enrollment, this patient had recently completed standard of care chemoradiation, and MRI revealed a peripherally enhancing, centrally necrotic mass in the right thalamus thought to represent a mixture of treatment-associated effects and residual tumor (Fig. 6A). [^{18}F]DASA-23 PET revealed two focal areas of radiotracer uptake, (Figs. 6B and C), with TBR max of 2.9 (Table 1). SUV distribution within the lesion and the SUV histogram are shown in Supplemental Fig. 9. H&E staining (Fig. 6D) and PKM2 IHC (Fig. 6E) confirmed the expression of PKM2 within the malignant biopsied tissue (also shown in Supplemental Fig. 9). Finally, we explored the ability of [^{18}F]DASA-23 to delineate a lower grade lesion, and administered [^{18}F]DASA-23 to one patient with WHO Grade III recurrent anaplastic astrocytoma (IC-4). IC-4 presented with a fluid filled cyst and surrounding patchy contrast enhancement within the left frontal lobe (Fig. 6F). The uptake of [^{18}F]DASA-23 was evident in this lesion, with a TBR max of 2.4 (Table 1). [^{18}F]DASA-23 uptake was heterogeneous within the lesion and the SUV distribution of the lesion is shown in Supplemental Fig. 10. H&E staining (Fig. 6I) and PKM2 IHC (Fig. 6J) confirmed the presence of PKM2 within the resected tumor tissue (Supplemental Fig. 10), the expression of PKM1 was also detected within this lesion.

Discussion

PKM2-specific imaging agents are sought after owing to their potential impact on clinical decision making and therapeutic monitoring in the setting of brain malignancies. PKM2 is overexpressed in many cancer types, including GBM, and is found in varying amounts in most body tissues with the exception of adult muscle, liver and brain. Given the absence of PKM2 in healthy brain, we set out to develop a clinically translatable radiotracer for non-invasive assessment of PKM2 status in GBM. Here, we developed and translated [^{18}F]DASA-23, to measure aberrantly expressed PKM2 in GBM cells in culture, animal models, and patients. This is the first study to evaluate a PKM2-specific PET tracer in humans.

In cell culture, [^{18}F]DASA-23 showed rapid and extensive uptake in all human GBM cell lines evaluated, including commercial cell lines (U87 and LN18) and patient-derived lines (GBM206 and TP459), with no variation in relation to IDH mutation and MGMT promoter methylation status (22). We have previously demonstrated the *in vitro* specificity of [^{18}F]DASA-23 through competition studies with TEPP-46 and by modulation of PKM2 expression with PKM2-specific siRNA (24, 31). Using mouse models, we highlight the ability of [^{18}F]DASA-23 to target U87-GFP/luc GBMs compared to [^{18}F]FDOPA, an established amino acid PET tracer explored in the clinical management of GBM patients (30, 32). We emphasize that the goal of this study was not to develop a comparatively better tracer for brain cancer diagnosis but rather to develop a novel tracer that can provide new and actionable information about the glycolytic state of brain cancer, while maintaining a TBR similar to established tracers. In the present work, we confirmed the *in vivo* specificity of [^{18}F]DASA-23 with PET imaging and autoradiography under blocking conditions with TEPP-46. These results build on our previous validation of [^{18}F]DASA-23 which demonstrated that mice stereotactically injected with AAV9-PKM2 showed a position correlation between PKM2 mRNA levels and [^{18}F]DASA-23 PET uptake (33). We further

confirmed specificity with the isotopologue, [^{11}C]DASA-23, by completing PET imaging studies in mice bearing orthotopic GBM under baseline and blocking conditions (23).

We successfully translated [^{18}F]DASA-23 for clinical applications under investigational new drug status. The estimated effective dose of [^{18}F]DASA-23 (23.5 ± 5.8 μSv/MBq) is comparable to other fluorine-18 radiotracers evaluated in GBM patients including [^{18}F]FPPRGD2 (39.6 ± 18.1 μSv/MBq) (34) and [^{18}F]-fluoro-ethyl-tyrosine (16.5 μSv/MBq) (35). An injected dose of 300 MBq exposes the patient to 7.1 mSv which is below the whole-body dose limit of 30 mSv (single dose) specified by the US FDA for research subjects. Radiometabolite analysis in healthy volunteers demonstrated that [^{18}F]DASA-23 remained intact in human plasma up to 5-min post intravenous administration and then underwent some degradation at the 10- and 30-min sampling time points (28). Although the identity of the radiometabolite found in the 10 and 30-min samples is unknown, radio-HPLC analysis signifies that this is likely a smaller, polar fragment and implies it will not be able to passively cross the blood-brain barrier. We noted higher background [^{18}F]DASA-23 signal within the cerebral white matter relative to gray matter, observed in both healthy volunteers and patients. There is no evidence of expression of PKM2 within myelinated axons (36-38), suggesting that the uptake of [^{18}F]DASA-23 is likely non-specific and potentially may be related to the lipophilicity and highly planar structure of the DASA-23 molecule.

We note that the uptake profile of [^{18}F]DASA-23 by the GBM in patient IC-1 is different than the uptake profile of [^{18}F]FDG by the same tumor (Fig. 4). The high background uptake of [^{18}F]FDG within the cerebral cortex makes it difficult to accurately visualize the boundaries of the tumor. In contrast, [^{18}F]DASA-23 delineates this lesion with high signal to background, and the uptake pattern of [^{18}F]DASA-23 is also different to that of [^{18}F]FDG. We observe the highest levels of [^{18}F]DASA-23 uptake at the posterior medial aspect of the tumor that additionally did not show substantial MRI contrast enhancement, highlighting the ability of [^{18}F]DASA-23 to cross the BBB and to provide information regarding the glycolytic status of the tumor independent of BBB integrity. We additionally demonstrate the lack of a metabolic response in IC-1 using [^{18}F]DASA-23 PET within one week of initiating TMZ and bevacizumab therapy. This was in comparison to contrast-enhanced MRI, which revealed a reduction in tumor volume after bevacizumab therapy, a phenomenon referred to as pseudoresponse (39, 40). The pattern of enhancement has been used as a surrogate for tumor grade and viability, however, processes that impact the permeability of the BBB will modify the degree and extent of enhancement, irrespective of the size and activity of the tumor (39, 41, 42). Bevacizumab is known to stabilize tumor vasculature and decrease BBB permeability, resulting in a reduction of tumor enhancement and pseudoresponse effect. Tumor progression was confirmed on a standard of care contrast-enhanced MRI three months later, highlighting the potential of PET imaging with [^{18}F]DASA-23 to identify a metabolic non-responder early on.

In patient IC-2 we observe the clear delineation of the GBM in the *corpus callosum* with contralateral extension on [^{18}F]DASA-23 PET. This tumor definition was more conspicuous compared to the heterogeneous T1-weighted MRI-based contrast enhancement. IC-2 was receiving bevacizumab at the time of [^{18}F]DASA-23 PET/MRI, which may account for the heterogeneous enhancement observed in IC-2. For all other patients evaluated in this pilot

study, the uptake of [^{18}F]DASA-23 in the intracranial tumors was evident and provided functional information regarding PKM2 status within these lesions. In patient IC-3, we observe the ability of [^{18}F]DASA-23 PET to visualize aberrant PKM2 expression and metabolic activity that can potentially aid in distinguishing viable tumor as opposed to treatment effects. Lastly, we highlight the ability of [^{18}F]DASA-23 to visualize aberrant PKM2 in anaplastic astrocytoma as seen in IC-4. Although the SUV in IC-4 was slightly higher than IC-3, we note that various factors can impact radiotracer uptake such as perfusion and necrosis, and this will be further investigated in future studies.

We developed this imaging strategy as a critical component of ongoing efforts to establish successful therapies for GBM. One important aspect of such efforts is to identify a reliable molecular imaging method to assess response to therapy. We previously reported the development of [^{18}F]FPPRG2 for evaluation of the integrin $\alpha_v\beta_3$ in GBM patients before and after bevacizumab therapy (43). Here, we describe the development of [^{18}F]DASA-23 to assess aberrant glycolysis in GBM. The effect of PKM2 activity in glycolysis and the proliferation of cancer cells has been shown to balance the production of biomolecular building blocks and the generation of pyruvate and ATP (17). Given the important role of aberrant metabolism in GBM growth and infiltration (44, 45), it is possible that most treatments for GBM would likely benefit from a general metabolic biomarker for treatment monitoring. The novelty of our ability to track PKM2 activity, which is a key regulator of GBM metabolism, lies in allowing us to potentially monitor different classes of therapies for metabolic response. We previously reported the ability of [^{18}F]DASA-23 to detect glycolytic changes in GBM cells in culture in response to multiple classes of anti-neoplastic agents (25). As an example of clinical translation of this concept, we highlight in this study the ability of [^{18}F]DASA-23 to identify IC-1 as a metabolic non-responder within one week of TMZ and bevacizumab therapy. We additionally confirm the ability of [^{18}F]DASA-23 to detect metabolic changes within IC-1 patient-derived recurrent GBM TP459 neurospheres in culture. That the [^{18}F]DASA-23 uptake in these neurospheres was comparable between control and TMZ IC_{50} conditions, may not be surprising given that the patient's GBM progressed on a TMZ-containing treatment regimen. Indeed, Park and colleagues had previously reported that TMZ-treated GBMs have reduced PKM2 expression (46).

We acknowledge some limitations, including the small number of patients evaluated to date in this pilot study, and the participation of patients at different stages of disease progression. We note the lack of certain parameters relating to DASA-23, including K_D and Bmax, which are currently under investigation. However, it should be noted that the primary aim of this study was the development and translation of a PKM2-specific radiopharmaceutical for evaluation of PKM2 status in GBMs. Future studies will evaluate the diagnostic accuracy of [^{18}F]DASA-23 in larger patient cohorts that include newly diagnosed and treatment-naïve patients.

In conclusion, we successfully developed and clinically translated [^{18}F]DASA-23 as a PKM2-specific radiotracer for non-invasive visualization of PKM2 status in brain cancer patients. [^{18}F]DASA-23 can be prepared with high radiochemical yield and molar activity suitable for clinical imaging, and is well tolerated by human subjects as determined in these initial studies. Of note, we observed significant binding of [^{18}F]DASA-23 in

brain tumors, with low background in healthy brain tissue. We additionally highlight the potential ability of [^{18}F]DASA-23 to identify early metabolic non-response to conventional chemotherapy and bevacizumab. Taken together, our results represent the first example of PKM2 visualization in human subjects. A comprehensive evaluation of [^{18}F]DASA-23 in larger patient populations is anticipated.

Supplementary Material

Refer to Web version on PubMed Central for supplementary material.

Acknowledgements.

We thank the Cyclotron and Radiochemistry Facility at Stanford University for the fluorine-18 production, in particular Dr. Fred Chin, and Carmen Azevedo. We thank the Small Animal Imaging facility at Stanford in particularly Drs. Timothy Doyle, Frezghi Habte and Laura Pisani. We thank Dr. Yuanyang Xie for helpful discussions about this study. This work was supported by the Ben and Catherine Ivy Foundation (Gambhir), GE Healthcare (Gambhir) and R01 CA216054-01 (Hayden Gephart). CB is grateful for support from Stanford School of Medicine Translational Research and Applied Medicine Fellowship and CBP acknowledges receipt of the Stanford Cancer Institute Fellowship Award for Cancer Research and NIH NINDS Research Education Grant (5R25NS065741-07). JQH acknowledges support from the NIH NCI (F30CA228215). We dedicate this manuscript to the loving memory of our mentor, Dr. Sanjiv Sam Gambhir.

References:

1. Gambhir SS. Molecular imaging of cancer with positron emission tomography. Nature reviews Cancer. 2002;2(9):683–93. [PubMed: 12209157]
2. Weissleder R Molecular Imaging in Cancer. Science (New York, NY). 2006;312(5777):1168.
3. Gambhir SS, Czernin J, Schwimmer J, Silverman DH, Coleman RE, and Phelps ME. A tabulated summary of the FDG PET literature. Journal of nuclear medicine : official publication, Society of Nuclear Medicine. 2001;42(5 Suppl):1s–93s.
4. Kelloff GJ, Hoffman JM, Johnson B, Scher HI, Siegel BA, Cheng EY, et al. Progress and Promise of FDG-PET Imaging for Cancer Patient Management and Oncologic Drug Development. Clinical Cancer Research. 2005;11(8):2785. [PubMed: 15837727]
5. Berti V, Mosconi L, and Pupi A. Brain: normal variations and benign findings in fluorodeoxyglucose-PET/computed tomography imaging. PET Clin. 2014;9(2):129–40. [PubMed: 24772054]
6. Chen W Clinical Applications of PET in Brain Tumors. Journal of Nuclear Medicine. 2007;48(9):1468–81. [PubMed: 17704239]
7. Albert NL, Weller M, Suchorska B, Galldiks N, Soffietti R, Kim MM, et al. Response Assessment in Neuro-Oncology working group and European Association for Neuro-Oncology recommendations for the clinical use of PET imaging in gliomas. Neuro-oncology. 2016;18(9):1199–208. [PubMed: 27106405]
8. Wester HJ, Herz M, Weber W, Heiss P, Senekowitsch-Schmidtke R, Schwaiger M, et al. Synthesis and radiopharmacology of O-(2-[18F]fluoroethyl)-L-tyrosine for tumor imaging. Journal of nuclear medicine : official publication, Society of Nuclear Medicine. 1999;40(1):205–12.
9. Weber WA, Wester HJ, Grosu AL, Herz M, Dzewas B, Feldmann HJ, et al. O-(2-[18F]fluoroethyl)-L-tyrosine and L-[methyl-11C]methionine uptake in brain tumours: initial results of a comparative study. European journal of nuclear medicine. 2000;27(5):542–9. [PubMed: 10853810]
10. Kläsner B, Buchmann N, Gempt J, Ringel F, Lapa C, and Krause BJ. Early [18F]FET-PET in Gliomas after Surgical Resection: Comparison with MRI and Histopathology. PloS one. 2015;10(10):e0141153. [PubMed: 26502297]
11. Chen W, Silverman DH, Delaloye S, Czernin J, Kamdar N, Pope W, et al. 18F-FDOPA PET imaging of brain tumors: comparison study with 18F-FDG PET and evaluation of diagnostic

accuracy. Journal of nuclear medicine : official publication, Society of Nuclear Medicine. 2006;47(6):904–11.

12. Patel CB, Fazzari E, Chakhoyan A, Yao J, Raymond C, Nguyen H, et al. (18)F-FDOPA PET and MRI characteristics correlate with degree of malignancy and predict survival in treatment-naïve gliomas: a cross-sectional study. Journal of neuro-oncology. 2018;139(2):399–409. [PubMed: 29679199]
13. Najjar AM, Johnson JM, and Schellingerhout D. The Emerging Role of Amino Acid PET in Neuro-Oncology. Bioengineering (Basel). 2018;5(4):104.
14. Lin J, Xia L, Liang J, Han Y, Wang H, Oyang L, et al. The roles of glucose metabolic reprogramming in chemo- and radio-resistance. J Exp Clin Cancer Res. 2019;38(1):218-. [PubMed: 31122265]
15. Dong G, Mao Q, Xia W, Xu Y, Wang J, Xu L, et al. PKM2 and cancer: The function of PKM2 beyond glycolysis. Oncol Lett. 2016;11(3):1980–6. [PubMed: 26998110]
16. Christofk HR, Vander Heiden MG, Harris MH, Ramanathan A, Gerszten RE, Wei R, et al. The M2 splice isoform of pyruvate kinase is important for cancer metabolism and tumour growth. Nature. 2008;452(7184):230–3. [PubMed: 18337823]
17. Zhang Z, Deng X, Liu Y, Liu Y, Sun L, and Chen F. PKM2, function and expression and regulation. Cell & Bioscience. 2019;9(1):52. [PubMed: 31391918]
18. Anastasiou D, Yu Y, Israelsen WJ, Jiang JK, Boxer MB, Hong BS, et al. Pyruvate kinase M2 activators promote tetramer formation and suppress tumorigenesis. Nature chemical biology. 2012;8(10):839–47. [PubMed: 22922757]
19. Zahra K, Dey T, Ashish, Mishra SP, and Pandey U. Pyruvate Kinase M2 and Cancer: The Role of PKM2 in Promoting Tumorigenesis. Frontiers in Oncology. 2020;10(159).
20. Israelsen William J, Dayton Talya L, Davidson Shawn M, Fiske Brian P, Hosios Aaron M, Bellinger G, et al. PKM2 Isoform-Specific Deletion Reveals a Differential Requirement for Pyruvate Kinase in Tumor Cells. Cell. 2013;155(2):397–409. [PubMed: 24120138]
21. Ostrom QT, Cioffi G, Gittleman H, Patil N, Waite K, Kruchko C, et al. CBTRUS Statistical Report: Primary Brain and Other Central Nervous System Tumors Diagnosed in the United States in 2012-2016. Neuro-oncology. 2019;21(Supplement_5):v1–v100. [PubMed: 31675094]
22. Mukherjee J, Phillips JJ, Zheng S, Wiencke J, Ronen SM, and Pieper RO. Pyruvate kinase M2 expression, but not pyruvate kinase activity, is up-regulated in a grade-specific manner in human glioma. PloS one. 2013;8(2):e57610. [PubMed: 23451252]
23. Witney TH, James ML, Shen B, Chang E, Pohling C, Arksey N, et al. PET imaging of tumor glycolysis downstream of hexokinase through noninvasive measurement of pyruvate kinase M2. Science translational medicine. 2015;7(310):310ra169.
24. Beinat C, Alam IS, James ML, Srinivasan A, and Gambhir SS. Development of [(18)F]DASA-23 for Imaging Tumor Glycolysis Through Noninvasive Measurement of Pyruvate Kinase M2. Molecular imaging and biology. 2017;19(5):665–72. [PubMed: 28236227]
25. Beinat C, Patel CB, Xie Y, and Gambhir SS. Evaluation of Glycolytic Response to Multiple Classes of Anti-glioblastoma Drugs by Noninvasive Measurement of Pyruvate Kinase M2 Using [18F]DASA-23. Molecular imaging and biology. 2019.
26. Beinat C, Haywood T, Chen YS, Patel CB, Alam IS, Murty S, et al. The Utility of [(18)F]DASA-23 for Molecular Imaging of Prostate Cancer with Positron Emission Tomography. Molecular imaging and biology. 2018;20(6):1015–24. [PubMed: 29736561]
27. James ML, Shen B, Zavaleta CL, Nielsen CH, Mesangeau C, Vuppala PK, et al. New positron emission tomography (PET) radioligand for imaging σ-1 receptors in living subjects. Journal of medicinal chemistry. 2012;55(19):8272–82. [PubMed: 22853801]
28. Beinat C, Patel CB, Haywood T, Shen B, Naya L, Gandhi H, et al. Human biodistribution and radiation dosimetry of [(18)F]DASA-23, a PET probe targeting pyruvate kinase M2. European journal of nuclear medicine and molecular imaging. 2020;47(9):2123–0. [PubMed: 31938892]
29. Ellingson BM, Bendszus M, Boxerman J, Barboriak D, Erickson BJ, Smits M, et al. Consensus recommendations for a standardized Brain Tumor Imaging Protocol in clinical trials. Neuro-oncology. 2015;17(9):1188–98. [PubMed: 26250565]

30. Pafundi DH, Laack NN, Youland RS, Parney IF, Lowe VJ, Giannini C, et al. Biopsy validation of 18F-DOPA PET and biodistribution in gliomas for neurosurgical planning and radiotherapy target delineation: results of a prospective pilot study. Neuro-oncology. 2013;15(8):1058–67. [PubMed: 23460322]

31. Acquadro E, Cabella C, Ghiani S, Miragoli L, Bucci EM, and Corpillo D. Matrix-assisted laser desorption ionization imaging mass spectrometry detection of a magnetic resonance imaging contrast agent in mouse liver. Analytical chemistry. 2009;81(7):2779–84. [PubMed: 19281170]

32. Humbert O, Bourg V, Mondot L, Gal J, Bondiau PY, Fontaine D, et al. (18)F-DOPA PET/CT in brain tumors: impact on multidisciplinary brain tumor board decisions. European journal of nuclear medicine and molecular imaging. 2019;46(3):558–68. [PubMed: 30612162]

33. Haywood T, Beinat C, Gowrishankar G, Patel CB, Alam IS, Murty S, et al. Positron emission tomography reporter gene strategy for use in the central nervous system. Proceedings of the National Academy of Sciences. 2019;116(23):11402.

34. Mittra ES, Goris ML, Iagaru AH, Kardan A, Burton L, Berganos R, et al. Pilot pharmacokinetic and dosimetric studies of (18)F-FPPRGD2: a PET radiopharmaceutical agent for imaging α(v)β(3) integrin levels. Radiology. 2011;260(1):182–91. [PubMed: 21502381]

35. Pauleit D, Floeth F, Herzog H, Hamacher K, Tellmann L, Muller HW, et al. Whole-body distribution and dosimetry of O-(2-[18F]fluoroethyl)-L-tyrosine. European journal of nuclear medicine and molecular imaging. 2003;30(4):519–24. [PubMed: 12589478]

36. Ravera S, and Panfoli I. Role of myelin sheath energy metabolism in neurodegenerative diseases. Neural Regen Res. 2015;10(10):1570–1. [PubMed: 26692843]

37. Brown AM, Wender R, and Ransom BR. Metabolic substrates other than glucose support axon function in central white matter. Journal of Neuroscience Research. 2001;66(5):839–43. [PubMed: 11746409]

38. Nijland PG, Michailidou I, Witte ME, Mizee MR, van der Pol SMA, van het Hof B, et al. Cellular distribution of glucose and monocarboxylate transporters in human brain white matter and multiple sclerosis lesions. Glia. 2014;62(7):1125–41. [PubMed: 24692237]

39. Arevalo OD, Soto C, Rabiei P, Kamali A, Ballester LY, Esquenazi Y, et al. Assessment of Glioblastoma Response in the Era of Bevacizumab: Longstanding and Emergent Challenges in the Imaging Evaluation of Pseudoresponse. Front Neurol. 2019;10:460. [PubMed: 31133966]

40. Chang JH, Kim C-Y, Choi BS, Kim YJ, Kim JS, and Kim IA. Pseudoprogression and pseudoresponse in the management of high-grade glioma : optimal decision timing according to the response assessment of the neuro-oncology working group. J Korean Neurosurg Soc. 2014;55(1):5–11. [PubMed: 24570811]

41. Brandsma D, and van den Bent MJ. Pseudoprogression and pseudoresponse in the treatment of gliomas. Current opinion in neurology. 2009;22(6):633–8. [PubMed: 19770760]

42. Boxerman JL, Zhang Z, Safriel Y, Rogg JM, Wolf RL, Mohan S, et al. Prognostic value of contrast enhancement and FLAIR for survival in newly diagnosed glioblastoma treated with and without bevacizumab: results from ACRIN 6686. Neuro-oncology. 2018;20(10):1400–10. [PubMed: 29590461]

43. Iagaru A, Mosci C, Mittra E, Zaharchuk G, Fischbein N, Harsh G, et al. Glioblastoma Multiforme Recurrence: An Exploratory Study of (18)F FPPRGD2 PET/CT. Radiology. 2015;277(2):497–506. [PubMed: 25965900]

44. Marie SKN, and Shinjo SMO. Metabolism and brain cancer. Clinics (Sao Paulo). 2011;66 Suppl 1(Suppl 1):33–43. [PubMed: 21779721]

45. Agnihotri S, and Zadeh G. Metabolic reprogramming in glioblastoma: the influence of cancer metabolism on epigenetics and unanswered questions. Neuro-oncology. 2016;18(2):160–72. [PubMed: 26180081]

46. Park I, Mukherjee J, Ito M, Chaumeil MM, Jalbert LE, Gaensler K, et al. Changes in pyruvate metabolism detected by magnetic resonance imaging are linked to DNA damage and serve as a sensor of temozolomide response in glioblastoma cells. Cancer research. 2014;74(23):7115–24. [PubMed: 25320009]

Translational Relevance:

Pyruvate kinase M2 (PKM2) catalyzes the final step in glycolysis, a key process of cancer metabolism. PKM2 is preferentially expressed by glioblastoma (GBM) cells with minimal expression in healthy brain, making it an important biomarker of cancer glycolytic re-programming. Our study describes the development, validation, and translation of a novel radiotracer ([^{18}F]DASA-23) for evaluation of aberrantly expressed PKM2 in GBM. First-in-human imaging studies in glioma patients demonstrate the effectiveness of [^{18}F]DASA-23 in detecting aberrantly expressed PKM2 and it was able to identify a metabolic non-responder within 1-week of treatment initiation. This is the first study to evaluate a PKM2-specific radiotracer in humans and has paved the way for a more comprehensive clinical trial of [^{18}F]DASA-23 in tumors, including brain tumors, and other indications that are marked by high levels of PKM2.

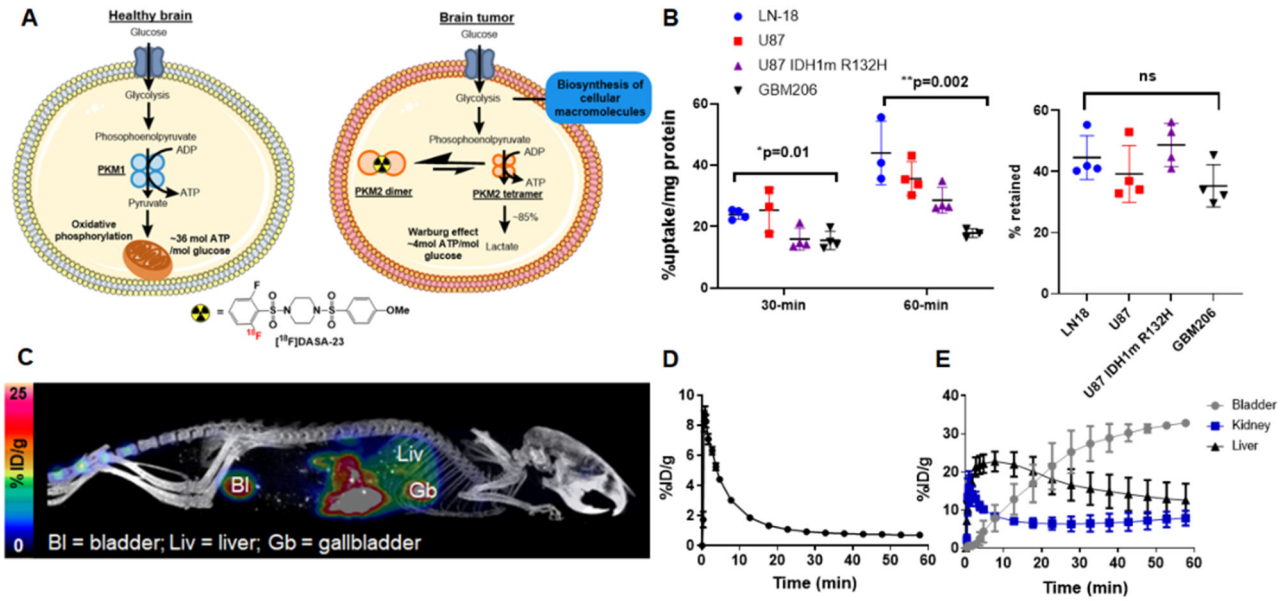

Figure 1.

Initial development of [^{18}F]DASA-23 as a PKM2 radiopharmaceutical. **A** Schematic illustrating the impact of PKM2 on tumor cell glycolysis. The PKM2 isoform is found in proliferating non-tumor and tumor cells. PKM1 is found in the healthy brain. Two quaternary PKM2 isoforms exist as homodimeric and homotetrameric forms (represented as orange circles). Dimeric PKM2 has a reduced affinity for phosphoenolpyruvate compared to tetrameric PKM2. Dimeric PKM2 predominates in tumor cells. A reduced conversion of phosphoenolpyruvate leads to a diminished production of pyruvate and allows the upstream accumulation of glycolytic intermediates that can support the biosynthesis of cellular macromolecules and production of new daughter cells. In contrast, PKM1 is found in the healthy brain and has high constitutive activity for phosphoenolpyruvate. **B** Cellular uptake and retention profile of [^{18}F]DASA-23 over time in a human glioma cell panel including LN18 (IDH1 wild-type, MGMT promoter unmethylated) U87 (IDH1 wild-type, MGMT promoter methylated), U87 IDH1 R132H (MGMT promoter methylated) and GBM206 (IDH1 wild-type, MGMT promoter methylated) cells. One-way ANOVA demonstrated significant differences in uptake across cell lines at the 30- and 60-min time points. Tukey's multiple comparisons of 30-min data revealed significant changes between U87 and U87 IDH1m R132H (p=0.04), and U87 and GBM206 cells (p=0.03). Tukey's multiple comparisons of 60-min data showed significant changes between LN18 and U87 IDH1 R132H (p=0.03,) LN18 and GBM206 (p=0.02), and U87 and GBM206 (p=0.02). **C** Representative maximum intensity projection (MIP) of [^{18}F]DASA-23 in a healthy mouse. Image is summed over 60-min. **D** Time activity curve of [^{18}F]DASA-23 in the healthy mouse brain showing initial uptake and then rapid clearance. **E** Time activity curves reflecting [^{18}F]DASA-23 renal and hepatobiliary clearance.

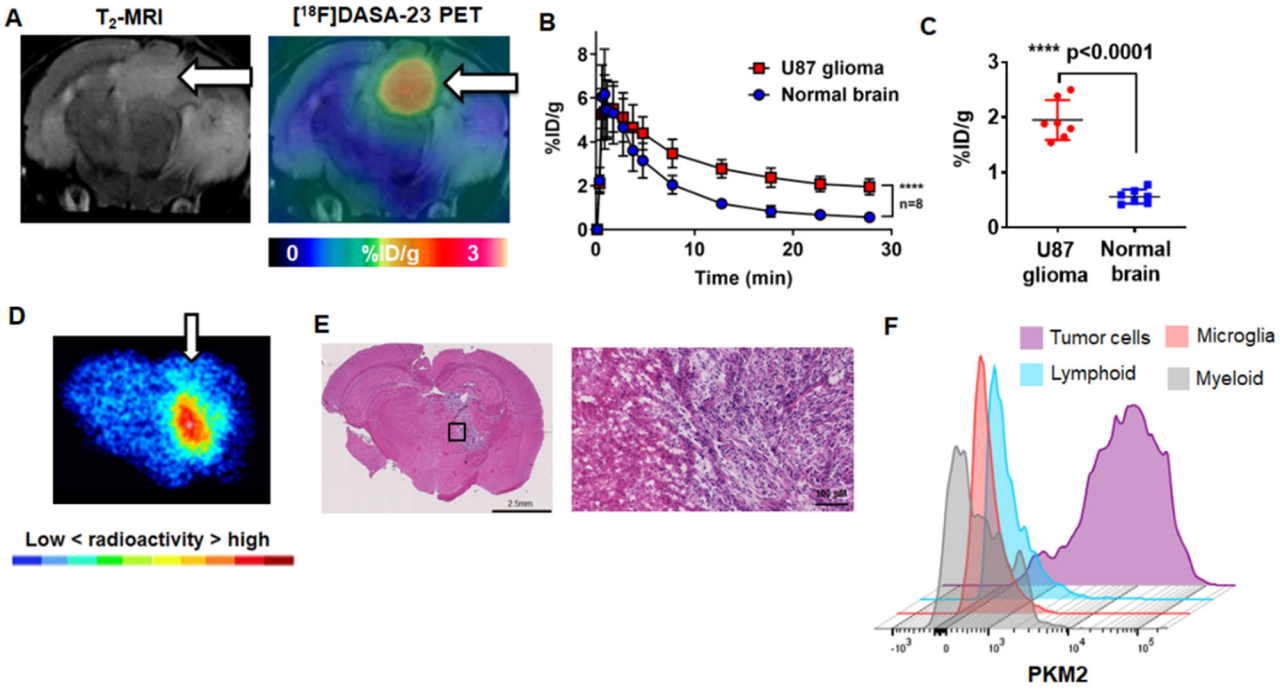

Figure 2.

Evaluation of [^{18}F]DASA-23 in orthotopic U87-GFP/luc GBM mice. **A** Representative images of a mouse bearing an orthotopic U87-GFP/luc GBM (white arrow), the presence of the tumor is confirmed with T2-weighted MRI. A representative [^{18}F]DASA-23 fused PET/CT/MR image is shown summed 10-30 min post tracer administration. **B** Time activity curves illustrating the uptake and clearance of [^{18}F]DASA-23 over time in the U87-GFP/luc GBM and contralateral normal brain, p<0.0001, n=8. **C** Quantification of [^{18}F]DASA-23 radioactivity in U87-GFP/luc GBM and contralateral normal brain at 30-min post tracer administration, t-test, p<0.0001, n=8. **D** Representative [^{18}F]DASA-23 autoradiography in mice bearing orthotopic U87-GFP/luc GBM at 30-mins post tracer administration. **E** H&E stain of an adjacent section showing the presence of the highly cellular GBM. **F** Expression profile of PKM2 in the brain of mice bearing orthotopic U87-GFP/luc GBM using flow cytometry (n=4).

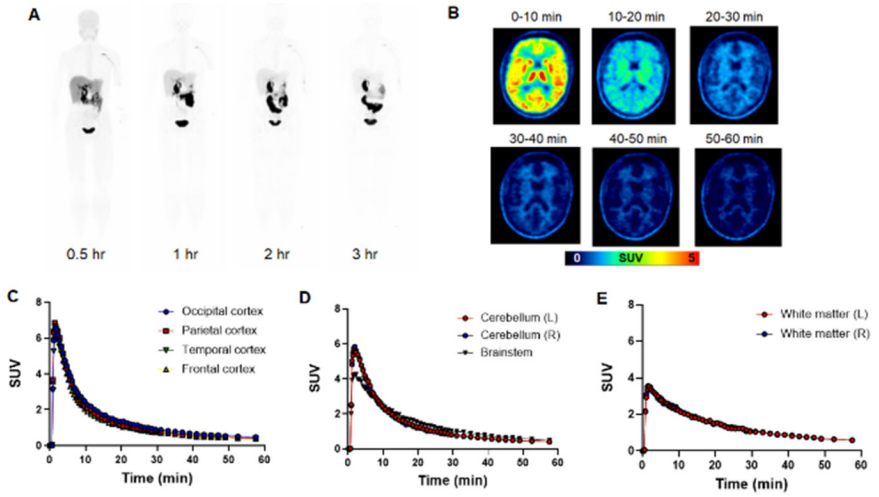

Figure 3.

Evaluation of [^{18}F]DASA-23 in healthy human volunteers. **A** Representative [^{18}F]DASA-23 whole body maximum intensity projections show the biodistribution of the PET tracer at various time points post tracer administration in volunteer 3. **B** Representative axial [^{18}F]DASA-23 PET images of a healthy human brain at various summed time points post tracer administration. **C** Time activity curves showing [^{18}F]DASA-23 uptake and clearance in the cerebral cortices, **D** posterior fossa and **E** white matter in the left (L) and right (R) brain hemispheres.

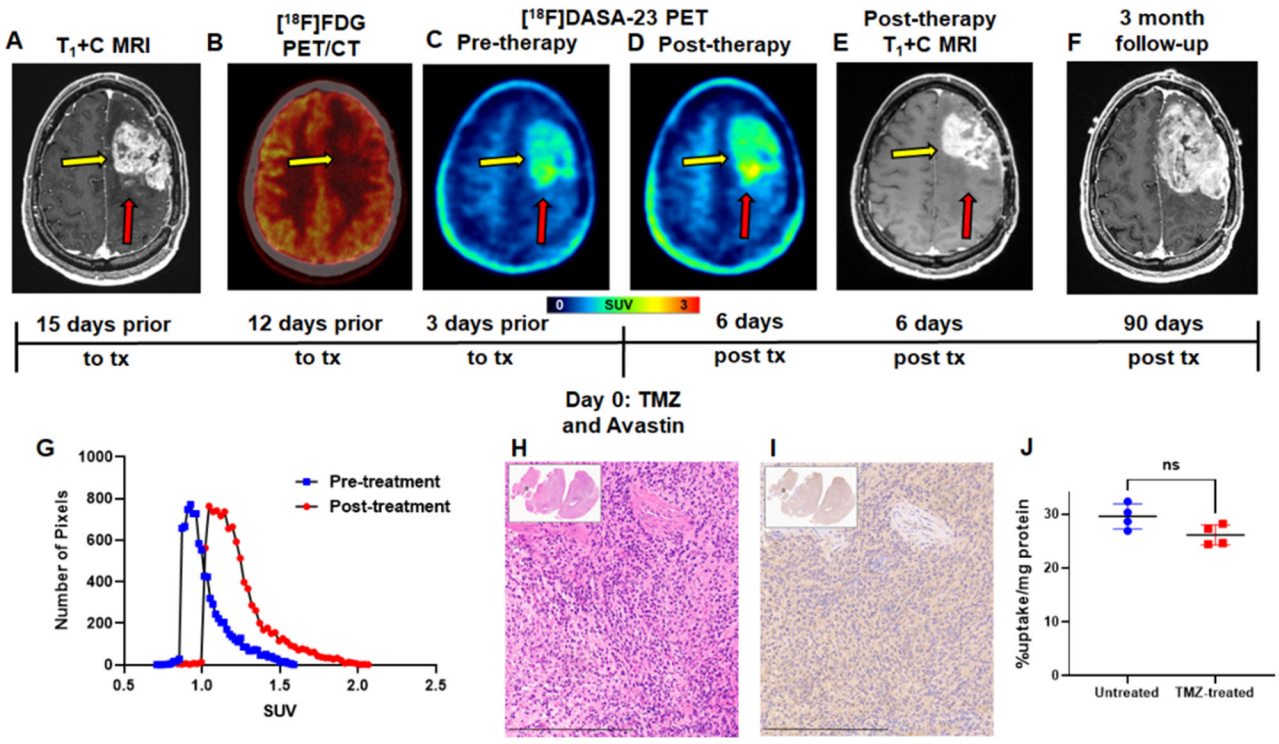

Figure 4.

Evaluation of serial [^{18}F]DASA-23 imaging in recurrent GBM patient IC-1. **A** Representative contrast-enhanced T1-weighted MRI shown in the axial plane. Yellow arrow indicates tumor, while red arrow indicates the posterior medial portion of the tumor that does not show substantial contrast enhancement. **B** [^{18}F]FDG PET/CT shown in the axial plane, yellow arrow indicates area of [^{18}F]FDG uptake corresponding to the area of contrast enhancement. This scan was obtained 9 days prior to the [^{18}F]DASA-23 PET scan. **C** Representative pre-therapy summed 30-60 min [^{18}F]DASA-23 PET, and **D** Representative post-therapy summed 30-60 min [^{18}F]DASA-23 PET, yellow arrow indicates tumor, red arrow indicates the posterior medial portion of the tumor that did not show substantial MRI contrast enhancement, but [^{18}F]DASA-23 uptake is evident. **E** Representative post-therapy contrast-enhanced T1-weighted MRI shown in the axial plane. **F** A subsequent standard of care contrast enhanced T1-weighted MRI is shown in the same axial plane and reveals tumor progression within the areas of [^{18}F]DASA-23 uptake at the medial and lateral posterior portions of the left frontal mass. **G** [^{18}F]DASA-23 SUV distribution within the lesion pre- and post-therapy. H&E **H** and PKM2 IHC **I** of the resected tumor tissue shown at 10×, scale bar indicates 300 μm. **J** Non-significant change (t-test) in cellular uptake of [^{18}F]DASA-23 in TP459 neurospheres derived from patient IC-2 following treatment with the IC_{50} dose of TMZ. TMZ = temozolomide, tx = treatment, ns = not significant.

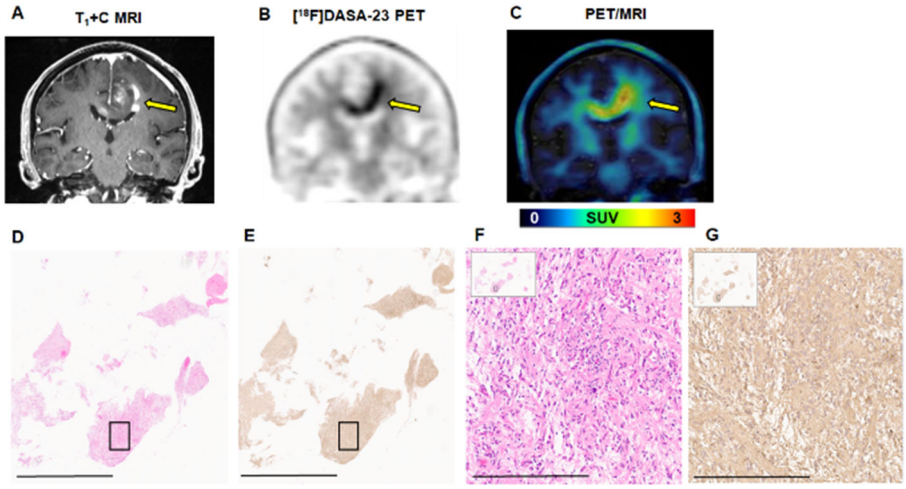

Figure 5.

Evaluation of [^{18}F]DASA-23 in GBM patient IC-2. **A** Representative contrast-enhanced T1-weighted MRI shown in the coronal plane. **B** Representative 30-60 min summed [^{18}F]DASA-23 PET shows high uptake of the radiotracer in the area corresponding to contrast enhancement. **C** Fused 30-60 min summed [^{18}F]DASA-23 PET/MRI. Yellow arrows indicate the location of the tumor. H&E staining (**D**) and PKM2 IHC (**E**) of the biopsied tissue shown at 0.4×, scale bar indicates 4mm. H&E (**F**) and PKM2 IHC (**G**) of the area shown within the black box in the insert confirm the expression of PKM2 within the malignant cells, images are shown at 10× and scale bar represents 300 μm.

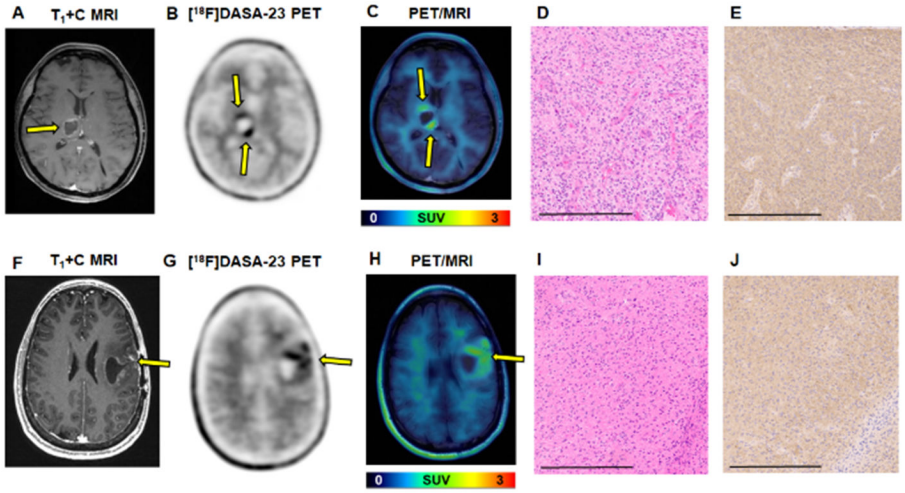

Figure 6.

Evaluation of [^{18}F]DASA-23 in patients IC-3 ((WHO Grade IV diffuse midline glioma, H3 K27M-mutant) and IC-4 (WHO grade III recurrent anaplastic astrocytoma). **A** Representative contrast-enhanced T1-weighted MRI of IC-3 shown in the axial plane. **B** Representative 30-60 min summed [^{18}F]DASA-23 PET shows two focal areas of tracer uptake in IC-3. **C** Fused 30-60 min summed [^{18}F]DASA-23 PET/MRI in IC-3. Yellow arrows indicate the location of the tumor. H&E **D** and PKM2 IHC **E** of the biopsied tissue confirm the expression of PKM2 within the malignant cells, images are shown at 10× and scale bar represents 300 μm. **F** Representative contrast-enhanced T1-weighted MRI of IC-4 shown in the axial plane. **G** Representative 30-60 min summed [^{18}F]DASA-23 PET shows heterogeneous tracer uptake in IC-4. **H** Fused 30-60 min summed [^{18}F]DASA-23 PET/MRI in IC-4. Yellow arrows indicate the location of the tumor. H&E **I** and PKM2 IHC **J** of the resected tumor confirm the expression of PKM2 within the malignant cells, images are shown at 10× and scale bar represents 300 μm.

Table 1.

[^{18}F]DASA-23 parameters in intracranial tumor patients

Patient	Tumor SUV	Tumor SUV max	White matter SUV	TBR	TBR max	Gray matter SUV	T/GM	T/GM max
IC-1 [^{18}F]FDG	5.7	8.2	2.8	2.0	2.9	10.0	0.57	0.82
IC-1 pre-therapy	1.4	1.6	0.62	2.3	2.6	0.46	3.0	3.5
IC-1 post-therapy	1.8	2.1	0.72	2.5	2.9	0.53	3.4	4.0
IC-2	2.0	2.2	0.78	2.6	2.8	0.49	4.1	4.5
IC-3	1.5	1.8	0.63	2.4	2.9	0.49	3.1	3.7
IC-4	1.5	2.0	0.82	1.8	2.4	0.64	2.3	3.1